JNeurosci
THE JOURNAL OF NEUROSCIENCE

Research Articles | Systems/Circuits

Cell-type- and subregion-specific basolateral amygdala inputs to ventral CA1–subiculum

https://doi.org/10.1523/JNEUROSCI.1041-26.2026

Received: 19 June 2026
Revised: 23 October 2026
Accepted: 1 November 2026

Copyright © 2026 the authors

This Early Release article has been peer reviewed and accepted, but has not been through the composition and copyediting processes.The final version may differ slightly in style or formatting and will contain links to any extended data.

Alerts: Sign up at www.jneurosci.org/alerts to receive customized email alerts when the fully formatted version of this article is published.

Cell-type- and subregion-specific basolateral amygdala inputs to ventral CA1–subiculum

Abbreviated title: Heterogeneity of amygdala–hippocampal circuit

Minghua Li (李明华)[1,*], Wanyi Guo (郭婉宜)[1,*], Yu-Qiu Jiang (姜玉秋)[1], Qian Sun (孙钱)[1,#]

[1]Department of Neurosciences, School of Medicine, Case Western Reserve University, 10900 Euclid Ave, Cleveland, OH 44106, USA

[*]Contributed equally

[#]Correspondence: Qian Sun (qxs111@case.edu)

Number of pages: 29

Number of figures: 8

Number of words for abstract: 230

Number of words for introduction: 624

Number of words for discussion: 1483

Conflict of interest statement: The authors declare no competing financial interests.

Acknowledgments: This work was supported by R01MH129294 and R01MH130367 from NIH (Q.S.) and institutional support from Case Western Reserve University (Q.S.).

JNeurosci Accepted Manuscript

ABSTRACT

The hippocampus is essential for learning and memory and interacts extensively with cortical and subcortical regions. Although the heterogeneity of intrinsic connectivity of hippocampal neurons is well established, the diversity of its extrahippocampal connectivity remains less understood. Such differential connectivity may contribute to functional diversity of hippocampal neurons in specific positions. Ventral CA1 (vCA1) and ventral subiculum (vSub) form strong reciprocal connections with the basolateral amygdala (BLA), a region critical for emotional and social regulation. Consequently, BLA–vCA1–vSub circuits have been implicated in anxiety-related and social behaviors. However, the functional connectivity from BLA to vCA1–vSub at the cellular and circuit levels is underexplored. To address this, we combined viral tracing with Channelrhodopsin-2 (ChR2)–assisted slice electrophysiology to examine BLA projections to vCA1–vSub in mice of either sex. We found that BLA inputs are not uniformly distributed along the transverse axis in vCA1-vSub. Instead, BLA selectively excites pyramidal neurons in distal vCA1–vSub while largely avoiding proximal vCA1 near CA2. BLA terminals strongly excited parvalbumin-expressing interneurons but only weakly recruited a small subset of somatostatin-expressing interneurons, generating robust disynaptic inhibitory synaptic currents in pyramidal neurons. Additionally, the same distal pyramidal neurons that receive BLA excitation also project back to the BLA. These findings reveal that BLA establishes cell-type- and subregion-specific excitatory connections within vCA1–vSub, highlighting a circuit architecture that may underlie functional heterogeneity in ventral hippocampal processing.

Keywords: ventral hippocampus, basolateral amygdala, CA1, subiculum, parvalbumin, somatostatin

JNeurosci Accepted Manuscript

SIGNIFICANCE STATEMENT

The hippocampus interacts extensively with cortical and subcortical regions, yet how long-range extrahippocampal inputs are organized across hippocampal subregions remains poorly understood. We examined projections from the basolateral amygdala (BLA) to the ventral hippocampus and found that BLA inputs selectively excite pyramidal neurons in distal ventral CA1 and ventral subiculum while largely avoiding proximal ventral CA1. BLA projections preferentially excite parvalbumin-expressing interneurons, provide disynaptic inhibition onto pyramidal neurons, and are reciprocally connected with the same pyramidal neurons in ventral CA1 and subiculum they excite. These findings reveal a highly selective connectivity pattern of amygdala–hippocampal circuits, providing a circuit framework for understanding how emotional information is routed through distinct ventral hippocampal pathways.

JNeurosci Accepted Manuscript

INTRODUCTION

The hippocampus plays an essential role in learning and memory and extensively interacts with numerous cortical and subcortical regions. While the dorsal hippocampus plays a pivotal role in spatial navigation and memory, the ventral hippocampus is more strongly involved in emotional processing, anxiety-related behaviors, and social behaviors (Fanselow and Dong, 2010; Kjelstrup et al., 2002; Moser et al., 1993; Strange et al., 2014). Although the mechanisms underlying dorsoventral functional diversity in the hippocampus are still not fully understood, its differential connectivity with cortical and subcortical regions likely contributes to this functional heterogeneity along the dorsoventral axis (Fanselow and Dong, 2010; Gergues et al., 2020). For example, the ventral, but not dorsal, hippocampus forms extensive reciprocal connections with the basolateral amygdala (BLA) (AlSubaie et al., 2021; Berretta et al., 2001; Felix-Ortiz et al., 2013; Felix-Ortiz and Tye, 2014; Kim and Cho, 2017, 2020; Li et al., 2025; Pikkarainen et al., 1999; Pitkanen et al., 2000; Xu et al., 2016; Yang and Wang, 2017). As the BLA is critical for emotion, anxiety, and social behaviors, but not spatial memory (Amaral, 2003; Janak and Tye, 2015; Sah et al., 2003; Sun et al., 2020b), the reciprocal interactions between BLA and ventral hippocampus are believed to play a crucial role in regulating emotion, fear, and social behaviors (Felix-Ortiz et al., 2013; Felix-Ortiz and Tye, 2014; Guo et al., 2025; Kim and Cho, 2017, 2020; Li et al., 2025; Pi et al., 2020; Xu et al., 2016). Surprisingly, despite extensive research on amygdala–hippocampal circuits, the functional connectivity from the BLA to the ventral hippocampus remains incompletely understood at the cellular and circuit levels. This study aims to address anatomical and physiological connectivity between BLA and CA1–subicullum in the ventral hippocampus.

We have recently identified a monosynaptic glutamatergic input from BLA that strongly excites CA3 pyramidal neurons in a cell-type- and subregion-specific manner (Li et al., 2025). Specifically, we found that BLA does not uniformly innervate CA3 pyramidal neurons along the transverse axis within the ventral hippocampus. Rather, BLA preferentially excites a subpopulation of distal ventral CA3 pyramidal neurons (adjacent to CA2) to modulate social behavior (Li et al., 2025). In addition to its projection to CA3, BLA is also known to send dense projections to hippocampal output regions—ventral CA1 (vCA1) and ventral subiculum (vSub) (Hintiryan et al., 2021; Pi et al., 2020; Pikkarainen et al., 1999; Pitkanen et al., 2000). Yet the functional connectivity of this pathway at the physiological level is poorly defined. For example, it is unknown whether BLA indiscriminately innervates vCA1–vSub neurons or preferentially targets a specific population of vCA1–vSub neurons. Given that pyramidal neurons in vCA1-

Neurosci Accepted Manuscript

vSub are highly diverse (Bienkowski et al., 2018; Cembrowski et al., 2016; Cembrowski and Spruston, 2019; Gergues et al., 2020), identification of postsynaptic targets of BLA would have important functional implications. Moreover, CA1 and subiculum regions comprise a diverse group of GABAergic interneurons that critically regulate activity in CA1 and subiculum (Freund and Buzsaki, 1996; Pelkey et al., 2017). The extent to which BLA inputs preferentially excite pyramidal neurons versus interneurons remains unclear. Moreover, it remains unknown whether BLA inputs indiscriminately target all CA1 interneurons or preferentially excite specific interneuron subtypes.

To address these questions, we employed adeno-associated virus (AAV)-based retrograde and anterograde neural tracing and Channelrhodopsin2 (ChR2)-assisted patch-clamp recording to examine the anatomy and function of the BLA–vCA1–vSub projections. Our results revealed previously unrecognized heterogeneous connectivity between BLA and pyramidal neurons in vCA1–vSub. We further discovered that BLA drives disynaptic inhibition in pyramidal neurons by preferentially exciting parvalbumin-expressing (PV^+) cells in vCA1 and vSub. Moreover, we demonstrated that the same pyramidal neurons in vCA1 and vSub both receive excitatory input from and project to the BLA, forming a reciprocally connected circuit motif.

MATERIALS AND METHODS

Animals

Wild-type mice (WT, stock number: 000664), PV-IRES-Cre (stock number: 017320), and SOM-IRES-Cre (stock number: 013044) were initially purchased from the Jackson Laboratory (JAX). All mice were housed and bred in the Animal Resource Center of Case Western Reserve University School of Medicine on a 12h/12h, light/dark cycle with ad libitum access to food and water. Both male and female mice of 2–6-month-old were used in anatomical tracing and electrophysiology experiments. The procedures described were conducted in accordance with the National Institutes of Health regulations and approved by the Institutional Animal Care and Use Committees (IACUC) at Case Western Reserve University.

Stereotactic viral injection

Mice were anesthetized by 5% isoflurane during the initial induction and were maintained by ~1.5% isoflurane during the procedures of viral injection. The body temperature of the mice was maintained around 37°C using a homeothermic heating pad. Carprofen (5

JNeurosci Accepted Manuscript

mg/kg) was injected subcutaneously prior to the surgery and lidocaine (10 mg/kg) was applied to the operative site to provide local anesthesia. Small burr holes were drilled in the skull guided by stereotaxic coordinates. 100-300 nl of high titer virus were injected through a glass pipette using Nano-injector at the speed of 1-2 nl/sec. The following coordinates were used: BLA (AP: -1.80 mm, ML: ±3.40 mm, DV: -4.80 mm), vCA1 (AP: -3.40 mm, ML: ±3.60 mm, DV: -3.30 mm). After injections, skin was sutured sterilely, and mice were closely watched until they woke up. Carprofen was given every 24 hours for another 2 days.

The following virus were used: AAVretro-hSyn-mCherry (100 nl, 1.90×10^{13} vg/ml, Addgene), AAVretro-Ef1a-Cre (100 nl, 1.39×10^{13} GC/ml, Salk), AAV2-CaMKII-hChR2-eYFP-WPRE (300 nl, 4.00×10^{12} GC/ml, UNC), AAVretro-Ef1a-mCherry-IRES-Cre (100 nl, 1.30×10^{13} vg/ml, Addgene), AAV2-Ef1a-DIO-hChR2-eYFP (300 nl, 4.00×10^{12} vg/ml, UNC), AAVretro-hSyn-HI-eGFP-Cre-WPRE-SV40 (100 nl, 1.90×10^{13} GC/ml, Addgene), AAV2-CaMKII-eYFP (300 nl, 5.10×10^{12} vg/ml, UNC).

Immunofluorescence

Mice were deeply anesthetized, perfused with phosphate buffered saline (PBS), followed by 4% paraformaldehyde (PFA). For coronal sections, whole brains were removed and post-fixed with 4% PFA overnight at 4℃. 45-μm sections were prepared on a vibratome (Leica VT1000S). For hippocampal sections, whole brains were removed. Hippocampi were dissected out immediately, post-fixed with 4% PFA overnight at 4℃, then mounted in 4% agarose in the following day and sliced from dorsal to ventral into 45-μm sections in a vibratome (Leica VT1200S). Free-floating whole brain sections or hippocampal sections were processed for immunofluorescence. After three 10 min washes in PBS, sections were incubated with blocking solution (PBS with 5% normal goat serum and 0.3% triton X-100) for 2 hours. Then sections were incubated in primary antibodies in incubating solution (PBS with 3% normal goat serum and 0.3% triton X-100) for 1-2 days at 4℃. The following primary antibody was used: chicken anti-GFP (1:500, Aves lab, Cat #: GFP-1020). After being rinsed three times, each time for 10 min in PBS, sections were moved to secondary antibodies in incubating solution for 2 hours at room temperature. The following secondary antibody was used: goat anti-chicken 488 (1:1000, Invitrogen, Cat #: A11039). After three 10 min washes in PBS, sections were incubated with DAPI (0.5 μg/ml, Invitrogen, D1306) for 20-30 min at room temperature. Then sections were rinsed in PBS for 3 × 10 min, before they were mounted with VECTASHIELD antifade mounting medium (Vector Laboratories, H-1000-10) on slides. The fluorescence images were obtained on a confocal microscope (Zeiss, LSM 800).

JNeurosci Accepted Manuscript

Brain slice electrophysiology

Mice were anesthetized with isoflurane and decapitated in accordance with institutional regulations. Brains were removed. Hippocampi were dissected out on ice and placed into ice-cold dissection solution containing (in mM): 10 NaCl, 195 sucrose, 2.5 KCl, 10 glucose, 25 $NaHCO_3$, 1.25 NaH_2PO_4, 2 Na-Pyruvate, 0.5 $CaCl_2$ and 7 $MgCl_2$. Then hippocampi were embedded in a block of pre-made 3-4% agarose and sliced on a vibratome (Leica VT1000s or VT1200s) in ice-cold dissection solution. Transverse hippocampal slices (400-μm-thickness) were cut from dorsal to ventral and transferred into 32℃ artificial cerebrospinal fluid (ACSF) containing (in mM): 125 NaCl, 2.5 KCl, 20 glucose, 25 $NaHCO_3$, 1.25 NaH_2PO_4, 2 Na-Pyruvate, 2 $CaCl_2$ and 1 $MgCl_2$ for 20-30 min. Then the slices were moved to room temperature for at least 1.5 hours before recording. Dissection solution and ACSF were saturated with 95% O_2 and 5% CO_2 (pH = 7.4). Electrophysiological recordings were performed at 31-32°C.

Whole-cell recordings were obtained from pyramidal neurons and interneurons in CA1 and subiculum using either “blind” or “visualized” technique under 4× or 40× objectives, as described previously (Jiang et al., 2024; Li et al., 2024; Li et al., 2025; Sun et al., 2021). Patch pipettes were pulled from borosilicate capillary glass using a P-1000 Micropipette Puller (Sutter Instruments, P-1000) and had resistances around 4-6 MΩ, filled with intracellular solution containing (in mM): 135 K-Gluconate, 5 KCl, 0.1 EGTA-Na, 10 HEPES, 2 NaCl, 5 ATP-Mg, 0.4 GTP-Na_2, 10 phosphocreatine-Na_2 (pH = 7.3-7.4, 280-290 mOsm). In some voltage-clamp recording experiments, Cs^+ based intracellular solution was used: 135 Cs-Methanesulfonate, 5 KCl, 0.1 EGTA-Na, 10 HEPES, 2 NaCl, 5 ATP-Mg, 0.4 GTP-Na_2, 10 phosphocreatine-Na_2 (pH = 7.3-7.4, 280-290 mOsm). 0.2-0.5% biocytin was included in the intracellular solution for post hoc staining. Resting membrane potential was measured immediately upon break-in. Neurons with resting potentials more depolarized than -55 mV for pyramidal neurons or -40 mV for interneurons upon break-in or with a series resistance above 30 MΩ were excluded from analysis. Liquid junction potential was not corrected. In voltage-clamp recording, neurons were held at -70 mV. The 470-nm, 2-ms blue light pulses of constant intensity (18 mW) from an LED light source (Thorlabs, LED4D294) driven by pClamp11 software were delivered via a 40× water-immersion objective placed above the slices, as described previously (Jiang et al., 2024; Kinney et al., 2025; Li et al., 2025). A single light pulse or a train of 10-20-Hz light stimulation protocol was applied. Drugs (20 μM DNQX, 50 μM DL-APV, 1 μM TTX, 100 μM 4-AP) were bath applied to ACSF. In current-clamp recording, PSPs and action potentials were measured at resting potential.

Neurosci Accepted Manuscript

Biocytin staining

After whole-cell recordings, slices were fixed in 4% PFA for 24-48 hours at 4℃. The fixed slices were then incubated in a blocking solution (PBS with 5% normal goat serum and 0.5% Triton X-100) for 2 hours at room temperature. Then, slices were incubated in Streptavidin Alexa Fluor 594 (1:500, Invitrogen, S11227) or Streptavidin Alexa Fluor 647 (1:500, Invitrogen, S32357) in incubating solution (PBS with 0.1% Triton X-100) for 2 days at 4℃. After three 10 min washes in PBS, sections were incubated with DAPI (0.5 μg/ml, Invitrogen, D1306) for 20-30 min at room temperature. Slices were rinsed three times before they were embedded in VECTASHIELD antifade mounting medium (Vector Laboratories, H-1900) on slides. Images were obtained on a confocal microscope (Zeiss, LSM 800).

Experimental Design and Statistical Analyses

Student's t test, Mann–Whitney U test, Kruskal–Wallis test, one-way ANOVA, two-way repeated-measures ANOVA, followed by Tukey's test or Bonferroni's test for multiple comparisons, or Chi-square test, Fisher's exact test and post-hoc pairwise comparisons were used as appropriate. Statistical analyses were performed using Excel for Microsoft 365 (Microsoft Corporation, Redmond, WA, USA), Igor Pro 8 (WaveMetrics, Lake Oswego, OR, USA), or OriginPro 2022b (OriginLab, Northampton, MA, USA). Electrophysiological data were analyzed using in-house functions in AxoGraph X or pClamp 11. All data are expressed as mean ± SEM, unless otherwise noted. $P < 0.05$ is considered statistically significant.

BLA axonal distribution was quantified using ChR2-eYFP fluorescence intensity. For transverse-axis analysis, a freehand line was drawn in SO from the subiculum to CA3c in ImageJ Fiji, and the fluorescence intensity profile was extracted. Intensity values were binned into 20–25 segments based on their distances to the subiculum, and the mean fluorescence intensity of each segment was calculated. Values were normalized to the segment with the highest fluorescence intensity in the ventral hippocampal section from the same animal. For radial-axis analysis, a line was drawn in CA1a from SO to SLM, and the fluorescence intensity profile was similarly extracted. Intensity values were grouped into 20 segments based on the distances to SO, averaged within each segment, and normalized to the segment with the highest fluorescence intensity along the radial axis.

BLA fiber intensity in CA1a, b, c was analyzed by dividing CA1 equally into three subregions along the transverse axis. Equal-sized circles were drawn and the eYFP fluorescence was averaged in each region. eYFP fluorescence was then normalized to CA1a

eNeuro Accepted Manuscript

within each section or normalized to the highest fluorescence intensity in ventral sections within each mouse. BLA fiber intensity in dorsal-ventral CA1 was analyzed by averaging the fiber intensity in CA1a, b, c within each section and normalizing to the highest eYFP fluorescence in the most ventral section. Hippocampi were divided into 7 equal-sized transverse segments along the longitudinal axis. One transverse section was randomly chosen from each segment to be quantified.

BLA fibers were densely distributed throughout the vCA1a–subiculum region. The boundary between CA1a and subiculum in the ventral hippocampus is not sharply defined and has been described as a gradual, overlapping anatomical transition (Kinman et al., 2026; Pachicano et al., 2025). Therefore, cells recorded from vCA1a and the adjacent subiculum were pooled for analysis.

RESULTS

BLA selectively projects to distal CA1 (CA1a) and subiculum in the ventral hippocampus

To examine BLA fiber distribution in CA1 and subiculum, we injected an AAV-ChR2-enhanced yellow fluorescent protein (eYFP) into the BLA, dissected hippocampi out, and cut the transverse sections along the dorsoventral axis (**Figure 1A-B**). Consistent with our previous observations (Li et al., 2025), BLA fibers, as indicated by eYFP intensity in stratum oriens (SO), primarily targeted distal CA1, distal CA3, and subiculum in the intermediate and ventral hippocampus (**Figure 1C-D**). In CA1–subiculum, BLA fibers increased progressively from dorsal to ventral, decreased from subiculum-CA1a to CA1c, and preferentially innervated SO and stratum pyramidale (SP) (**Figure 1C-E**).

To selectively target CA1-projecting BLA neurons, we injected AAVretro-Cre-mCherry into vCA1, followed by a second Cre-dependent AAV-ChR2-eYFP injection into BLA (**Figure 2A**). Three weeks later, we either cut coronal sections (**Figure 2B**) or dissected out hippocampi and cut the transverse sections along the longitudinal (dorsoventral) axis, as we described previously (Li et al., 2025) (**Figure 2C**). We then calculated the strengths of BLA projections by measuring and quantifying the ChR2-eYFP fluorescence intensity as a proxy along all three anatomical axes in the hippocampus, including longitudinal, transverse, and radial axes (**Figure 2D-I**). We found that the fiber distributions from CA1-projecting BLA neurons were highly heterogeneous in the hippocampus along all three axes. Consistent with previous findings (Felix-Ortiz et al., 2013; Hintiryan et al., 2021; Pikkarainen et al., 1999; Pitkanen et al., 2000), BLA fibers were enriched in CA1 and subiculum in the ventral hippocampus, progressively

JNeurosci Accepted Manuscript

increasing from dorsal to ventral (**Figure 2D-G**). Interestingly, within the intermediate and ventral hippocampus, BLA fibers did not uniformly target CA1 and subiculum along the transverse axis. Instead, we found that BLA fibers were mostly distributed in distal CA1 (CA1a) and subiculum, with a significant weaker expression in proximal CA1 (CA1c) that is close to CA2 (**Figure 2D-F, H**). Moreover, along the radial axis in vCA1a, BLA fibers were mostly concentrated in SO/SP and were weakly distributed in stratum lacunosum-moleculare (SLM) (**Figure 2D-F, I**). Overall, these results provided anatomical evidence that BLA preferentially targeted a selective population of neurons located in distal CA1 and subiculum in the ventral hippocampus.

BLA excites distal vCA1 and vSub, but not proximal vCA1

To investigate the functional connections between BLA and vCA1–vSub, we employed ChR2-assisted slice electrophysiology by expressing ChR2 into BLA (**Figure 3**). Given the dense BLA innervation in distal vCA1 (vCA1a)–vSub, we first focused on examining the connections between BLA and pyramidal neurons in vCA1a–vSub (**Figure 3B-C**). Light pulses induced optically-evoked EPSCs (oEPSCs) in all vCA1a–vSub cells tested (**Figure 3D**, n = 26/26 cells). Moreover, oEPSCs were eliminated by bath application of DNQX (20 μM) and DL-APV (50 μM) (n = 5 cells, **Figure 3E**), indicating that BLA-vCA1/vSub synapses are glutamatergic. The latency of oEPSC onset following light stimulation was very short (1.92 ± 0.11 ms, n = 16 cells), consistent with monosynaptic connection. Bath application of tetrodotoxin (TTX, 1 μM) completely abolished oEPSCs, which were rescued by application of both TTX and 4-aminopyridine (4-AP, 100 μM), a voltage-gated potassium channel blocker (n = 6 cells, **Figure 3F**). As polysynaptic light-evoked synaptic transmission mediated by action potentials should have been blocked by TTX, the addition of 4-AP can only rescue monosynaptic transmitter release by directly boosting depolarization at $ChR2^{+}$ presynaptic terminals contacting postsynaptic sites (Petreanu et al., 2009).

Given the sparse BLA fibers in proximal vCA1 (**Figures 1,2**), we next asked if BLA differentially excites distal versus proximal vCA1. To control variations of viral expression across different animals, we recorded and compared pairs of pyramidal neurons from distal and proximal vCA1 in the same slices (**Figure 3G-I**). We found that in the same slices light pulses elicited large oEPSCs in vCA1a–vSub pyramidal neurons but produced minimal oEPSCs in proximal ventral CA1 (vCA1c) (n = 5 pairs, p = 0.024, paired t test, **Figure 3H-I**). Overall, these results demonstrated that BLA preferentially makes monosynaptic glutamatergic connections onto pyramidal neurons in distal vCA1 and vSub, but not in proximal vCA1.

JNeurosci Accepted Manuscript

BLA input activates interneurons to drive disynaptic inhibition in pyramidal neurons in vCA1–vSub

Next, we asked if stimulation of BLA terminals could also drive disynaptic inhibition in pyramidal neurons in vCA1–vSub (**Figure 4**). We performed voltage-clamp recording to measure both oEPSC (holding potential = -70 mV) and optically-evoked IPSC (oIPSC, holding potential = 0 mV) from the same cells using cesium-based intracellular solution. We found that light pulses elicited both oEPSC and oIPSC in all cells tested (100%, 7/7 cells, oEPSC = 229.72 ± 58.26 pA, oIPSC = 794.44 ± 189.74 pA, **Figure 4A,B**), resulting in an I/E ratio of 4.83 ± 1.42 (n = 7 cells, **Figure 4B**). The oEPSC latency was very short (1.926 ± 0.236 ms, n = 7 cells), consistent with monosynaptic connections. By contrast, the latency of oIPSC response was significantly longer (3.236 ± 0.286 ms, $p < 0.01$, paired t test, n = 7 cells, **Figure 4C,D**), indicating disynaptic inhibitory connections. In addition, bath applications of glutamatergic antagonists, DNQX and DL-APV, eliminated oIPSC (baseline oIPSC = 892.89 ± 191.93 pA, DNQX/APV = 10.15 ± 4.20 pA, n = 6 cells, $p < 0.01$, paired t test, **Figure 4E,F**). These results strongly suggest that the inhibitory responses in pyramidal neurons in vCA1–vSub resulted from the disynaptic inhibition mediated by suprathreshold spikes in interneurons evoked by light pulses.

Next, we asked whether BLA makes direct excitatory connections onto interneurons in vCA1–vSub. To address this, we used both wild-type (WT) mice and an interneuron-specific mouse line (**Figure 5A**). To identify GABAergic interneurons in vCA1–vSub, we targeted tdTomato to interneurons by crossing a vesicular GABA transporter (vGAT)-Cre line with a Ai9 tdTomato reporter line to generate vGAT-tdTomato mice. Cre-independent AAV-ChR2-eYFP was injected bilaterally into BLA in WT or vGAT-tdTomato mice, and we performed whole cell recordings on interneurons in vCA1a and vSub 3-4 weeks after viral injection (**Figure 5A**). vGAT-tdTomato mice allowed us to directly visualize and record GABAergic neurons labeled by tdTomato (**Figure 5B**). In the WT mice, interneurons were identified based on their cell body location in SO or SR. Additionally, the firing patterns and post hoc biocytin staining enabled us to further differentiate interneurons from pyramidal neurons with a high degree of confidence (**Figure 5B,C**). Given that BLA fibers were more densely distributed in SO, SP, and stratum radiatum (SR), we focused on interneurons located in these layers. The data from WT and vGAT-tdTomato mice were comparable and thus were combined. As expected, interneurons in vCA1–vSub displayed diverse intrinsic membrane properties, ranging from fast spiking to regular spiking (**Figure 5C**). We detected light-evoked excitatory synaptic responses in a

Neurosci Accepted Manuscript

majority of interneurons in vCA1–vSub (78.05%, 32/41 cells), with a mean oEPSC amplitude of 67.57 ± 24.46 pA (n = 32 cells). Interestingly, we noted that the latencies of oEPSC onsets of individual cells were highly variable, ranging from 1.10 to 11.93 ms (**Figure 5D**). In 65.63% of responsive cells (21/32 cells), the latency of oEPSC onsets was <3 ms (1.82 ± 0.10 ms, n = 21 cells), consistent with monosynaptic connections. In the remaining responsive cells (34.38%, 11/32 cells, **Figure 5E**), the latency ranged from 3.85 to 11.93 ms with a mean of 6.97 ± 0.91 ms (n = 11 cells, $p = 1.1 \times 10^{-8}$, unpaired t test, **Figure 5E**), indicating polysynaptic connections. Moreover, trial-to-trial variability in the latency of oEPSC onsets appeared higher in cells with longer latency, supporting polysynaptic connections (**Figure 5D**). Thus, in a subset of cells we further quantified the jitter of oEPSC onsets, defined as the standard deviation (SD) of oEPSC onset latencies across trials. We found that cells with longer latency displayed significantly a greater jitter (1.15 ± 0.28 ms, n = 5 cells, **Figure 5F**), compared to cells with shorter latency (0.21 ± 0.04 ms, n = 11 cells, p = 0.00021, unpaired t test, **Figure 5F**). Finally, a train of 20 Hz light stimulation evoked action potentials in 21.62% of interneurons (8/37 cells; **Figure 5G–H**), and all eight spiking cells exhibited short oEPSC onset latencies (<3 ms). Notably, the oEPSC amplitude was significantly larger in cells that exhibited light-evoked spiking than in cells that did not (spiking: 179.84 ± 88.83 pA, n = 8 cells; non-spiking: 28.05 ± 5.06 pA, n = 12 cells; p = 0.00137, Mann-Whitney test). These data indicate that the strength of the optically evoked synaptic response is associated with the ability of the afferent pathway to drive postsynaptic spiking. Overall, these results suggest that vCA1–vSub interneurons were activated by BLA inputs through both monosynaptic and polysynaptic excitation.

BLA input preferentially excites PV$^+$, but not somatostatin-expressing (SOM$^+$), cells

The above results demonstrated the excitatory connections between BLA and interneurons in vCA1–vSub. Interneurons in vCA1–vSub are highly diverse, comprising more than 20 subtypes (Harris et al., 2018; Klausberger and Somogyi, 2008; Pelkey et al., 2017). Thus, we next sought to investigate specific CA1 interneuron subtypes that are excited by BLA inputs using interneuron-specific Cre driver lines. We decided to focus on two major interneuron subtypes, PV$^+$ and SOM$^+$ cells, for the following two reasons. First, PV$^+$ and SOM$^+$ cells constitute two of the most prominent and abundant interneuron subtypes with respective Cre knock-in mouse lines available. Second, the positions of PV$^+$ and SOM$^+$ cells are mostly located in SO, SP, and SR, significantly overlapping with the dense BLA fibers in the same area. To identify PV$^+$ or SOM$^+$ cells, we crossed PV-Cre or SOM-Cre lines with a reporter line (Ai9) to

JNeurosci Accepted Manuscript

label PV^+ or SOM^+ cells with tdTomato, as previously described (Jiang et al., 2024; Kinney et al., 2025; Li et al., 2023).

In PV-td mice, we validated that all $tdTomato^+$ cells displayed fast-spiking firing patterns with short AP duration, a distinct feature of PV cells (maximum firing rate = 235.90 ± 23.87 Hz, AP half-width = 0.299 ± 0.025 ms, n = 20 cells, **Figure 6A-C**). We detected light-evoked putative monosynaptic excitatory responses (oEPSC = 726.82 ± 282.25 pA, n = 14 cells) in a majority of PV^+ cells (70%, 14/20 cells, **Figure 6F-G**) with a short oEPSC latency (1.60 ± 0.14 ms, n = 14 cells). The oEPSC amplitude in PV^+ cells was significantly greater than putative monosynaptic connections in interneurons that were recorded randomly ($p = 0.041$, rank sum test, **Figure 6G**). To confirm monosynaptic connections, we performed a pharmacology experiment using TTX and 4-AP. oEPSCs were completely blocked by bath application of TTX and were fully rescued by bath application of both TTX and 4-AP (n = 4 cells, **Figure 6E**). Another 3 PV^+ cells displayed putative polysynaptic responses (oEPSC = 82.75 ± 50.93 pA, n = 3 cells) with a longer latency (4.96 ± 1.29 ms). Moreover, single light pulses elicited action potentials in a majority of PV^+ cells (55%, 11/20 cells), compared to just 21.62% cells (8/37 cells) in interneurons recorded randomly (**Figure 6H**). Similarly, the probability of spikes induced by a train of 20-Hz stimulation was significantly higher in responsive PV^+ cells than responsive interneurons (Figure 6I-J). Taken together, these results suggest that the BLA input makes powerful monosynaptic excitatory connections onto PV^+ cells to drive action potential output.

Given a substantial topographical overlap between BLA terminal distribution and somatodendritic structures of SOM^+ cells in SO and SP, next we examined the connections between BLA and SOM^+ cells in vCA1–vSub. We performed whole cell recording on the visually identified $tdTomato^+$ cells using SOM-tdTomato mice, as we described previously (Jiang et al., 2024) (**Figure 7A-B**). Consistent with previous findings (Chamberland et al., 2024; Losonczy et al., 2002), intrinsic membrane properties of SOM^+ cells in vCA1–vSub were diverse (**Figure 7C**). Interestingly, we found that the connectivity probability between BLA and SOM^+ cells was relatively low. Only a minority of SOM^+ cells receive putative monosynaptic excitatory inputs from BLA (31.25%, 5/16 cells, oEPSC latency = 1.82 ± 0.16 ms), compared to the BLA-PV^+ connectivity rate at 75% (**Figure 7F**). Among these connected cells, oEPSC amplitude in SOM^+ cells was relatively small (106.13 ± 76.91 pA, n = 5 cells, **Figure 7G**). One additional SOM^+ cell displayed putative polysynaptic excitatory response (oEPSC = 31.84 pA) with a prolonged oEPSC latency of 6.87 ms. In addition, action potentials could only be elicited in 2 out of 16 SOM^+ cells (12.5%), compared to 55% in PV^+ cells (**Figure 7E, H**). Notably, no significant

Neurosci Accepted Manuscript

differences in resting membrane potential were detected across the interneuron populations examined (SOM^+: −53.99 ± 2.20 mV, n = 16 cells; PV^+: −55.40 ± 1.90 mV, n = 20 cells; all interneurons: −55.31 ± 1.38 mV, n = 41 cells), indicating that their ability to fire action potentials was not driven by differences in resting membrane potential. Overall, we concluded that the BLA input strongly excites PV^+ cells and only weakly excites a small subset of SOM^+ cells in vCA1–vSub.

Same pyramidal neurons in vCA1a–vSub both receive excitation from and project to BLA

The above results demonstrated that BLA excites a selective population of pyramidal neurons and interneurons in vCA1–vSub in a cell-type- and subregion-specific manner. Notably, pyramidal neurons in vCA1–vSub are also known to send reciprocal projections to BLA (Kim and Cho, 2017, 2020; Pitkanen et al., 2000; Xu et al., 2016). This raises an interesting question of whether the same pyramidal neurons in vCA1–vSub that receive direct excitation from BLA also project back to BLA (**Figure 8A**).

To address this question, we first performed a retrograde tracing experiment to examine cells in vCA1–vSub that project to BLA. A retrograde tracer, Cholera Toxin Subunit B (CTB), was bilaterally injected into BLA, and mice were sacrificed 7 days later for histology. We found an abundant expression of CTB^+ cells in vCA1–vSub, but not in dorsal CA1 (dCA1, n = 4, data not shown), consistent with the previous findings that vCA1-vSub neurons project extensively to BLA (Hintiryan et al., 2021; Pikkarainen et al., 1999; Pitkanen et al., 2000). Next, we performed a two-color dual anterograde-retrograde tracing experiment, in which we injected a mixture of AAVretro-H2B-mCherry and AAV-ChR2-eYFP into BLA (**Figure 8B**). In this experiment, the cells in vCA1–vSub projecting to BLA would be labelled by mCherry and BLA fibers in vCA1–vSub would be labeled by ChR2-eYFP (**Figure 8C**). The level of overlap between $mCherry^+$ cells and ChR2-$eYFP^+$ fibers in the hippocampus would indicate that the neurons that receive BLA inputs also project back to BLA. We observed numerous retrogradely labeled $mCherry^+$ cells in vCA1–vSub, but not in dCA1 (**Figure 8D**). Interestingly, a close inspection of hippocampal sections from different Bregma revealed a significant but incomplete overlap between ChR2-eYFP fibers and $mCherry^+$ cells (**Figure 8D**). In more ventral coronal sections, we observed a large overlap between ChR2-eYFP fibers and $mCherry^+$ cells in vCA1–vSub (**Figure 8E**).

The dual anterograde-retrograde results raise the possibility that pyramidal neurons in vCA1a–vSub may both receive input from and send projections to BLA. To test this at the

JNeurosci Accepted Manuscript

functional level, we injected a mix of AAVretro-H2B-mCherry and AAV-ChR2-eYFP into BLA bilaterally and performed whole cell recordings on BLA-projecting mCherry$^+$ cells in vCA1–vSub 3-4 weeks after viral injection (**Figure 8F-J**). We focused on mCherry$^+$ cells in distal vCA1–vSub, because BLA fibers were densely expressed in this area, with 72.69 ± 0.68% of vSub/CA1a cells labeled by mCherry (n = 3 sections/2 mice) (**Figure 8F**). All mCherry$^+$ cells displayed regular-spiking or bursting firing patterns that were consistent with pyramidal neurons in CA1 or subiculum (**Figure 8H**, n = 10 cells). Importantly, we detected light-evoked excitatory synaptic responses in all mCherry$^+$ cells in vCA1a–vSub tested (oEPSC = 83.31 ± 20.36 pA, n = 10/10 cells, **Figure 8I-J**). This data suggests that pyramidal neurons in vCA1a–vSub both receive excitation from BLA and send reciprocal projections to BLA.

DISCUSSION

Although BLA provides dense input to the ventral hippocampus (Felix-Ortiz et al., 2013; Felix-Ortiz and Tye, 2014; Pi et al., 2020; Pikkarainen et al., 1999; Pitkanen et al., 2000), its functional connectivity at the cellular and circuit levels remains incompletely understood. Our study provides evidence that BLA projections to ventral CA1 and subiculum are not uniform topographically, with preferential innervation of distal CA1 and subiculum and minimal input to proximal CA1 adjacent to CA2. We further show that BLA terminals strongly excite PV$^+$ interneurons, generating feedforward inhibition of CA1 and subicular pyramidal neurons. Moreover, distal vCA1 and vSub pyramidal neurons receiving BLA excitation also project back to BLA, revealing a reciprocal connected circuit motif. Together with our recent work on topographic heterogeneity of BLA–CA3 connectivity (Li et al., 2025), these findings reveal heterogeneous BLA inputs across pyramidal neurons and interneuron subtypes in the ventral hippocampus, potentially contributing to functional diversity of hippocampal processing.

Heterogeneous connectivity between BLA and ventral hippocampus

BLA sends dense projections to the ventral, but not dorsal, hippocampus (Pikkarainen et al., 1999; Pitkanen et al., 2000; Yang and Wang, 2017). The BLA-ventral hippocampus circuits are critically involved in contextual fear memory, anxiety-related behaviors and social behaviors (Felix-Ortiz et al., 2013; Felix-Ortiz and Tye, 2014; Guo et al., 2025; Li et al., 2025; Pi et al., 2020; Xu et al., 2016). It is, however, less clear how BLA input modulates hippocampal neuron activity at the cell and circuit levels. We have previously reported that BLA selectively projects to distal CA3 pyramidal neurons in the ventral hippocampus (Li et al., 2025). Here, we extended our previous findings by focusing on the projection from BLA to hippocampal output regions

JNeurosci Accepted Manuscript

CA1 and subiculum. Our results show that BLA does not uniformly innervate all vCA1 or subicular neurons, but rather selectively targets distal vCA1 and vSub and largely avoid making monosynaptic connections with proximal vCA1 adjacent to CA2.

It is worth noting that CA1 and subicular neurons in the ventral hippocampus are highly heterogeneous (Bienkowski et al., 2018; Cembrowski et al., 2016; Cembrowski and Spruston, 2019; Gergues et al., 2020; Yao et al., 2021). Ventral CA1 pyramidal neurons in different anatomical positions are differentially connected with extrahippocampal regions and are associated with different behaviors (Fanselow and Dong, 2010; Meira et al., 2018; Okuyama et al., 2016). Notably, dorsal CA2 (dCA2), a hippocampal subregion essential for social behaviors (Alexander et al., 2016; Dudek et al., 2016; Hitti and Siegelbaum, 2014; Oliva et al., 2020), preferentially targets distal, but not proximal, vCA1 (Meira et al., 2018). Thus, dCA2 and BLA appear to target the same vCA1 subregion. Given that both the dCA2–vCA1 circuit (Cope et al., 2023; Meira et al., 2018; Okuyama et al., 2016; Watarai et al., 2021) and the BLA–vCA1 circuit (Felix-Ortiz and Tye, 2014; Xiong et al., 2024) are critically involved in social behaviors, we propose that distal CA1 and subiculum may integrate convergent inputs from dCA2 and BLA to contribute to social behaviors. Overall, our findings reveal heterogeneous BLA–ventral hippocampal connectivity that may support emotional and social behaviors.

BLA-CA1 interneuron connections

A previous study indicates that the disynaptic inhibition in vCA1 pyramidal neurons can be elicited by stimulating BLA terminals, raising the possibility that BLA also excites interneurons (Felix-Ortiz et al., 2013). However, cell identities of interneurons targeted by BLA are unknown. Here we confirmed that activation of BLA terminals drives robust disynaptic feedforward inhibition in vCA1–vSub pyramidal neurons, with an I/E ratio of 3-4. The value is in line with I/E ratios reported in Schaffer collateral pathway in CA1 pyramidal neurons, recurrent collateral pathway in CA3 pyramidal neurons, and other cortical neurons (Pouille et al., 2009; Pouille and Scanziani, 2001, 2004; Sun et al., 2017). Our measurement of I/E ratio relied on non-physiological conditions to increase the driving force of chloride. Future work is needed to clarify the effect of BLA-driven feedforward inhibition on pyramidal neuron output under physiological conditions.

We identified PV^+, but not SOM^+, interneurons as a major target of BLA input and the excitatory synapses between BLA-PV^+ interneurons are powerful. Activation of this synapse is sufficient to elicit spikes in a majority of PV^+ interneurons. Because of the significant overlap

JNeurosci Accepted Manuscript

between SOM$^+$ interneuron somatodendritic structures and BLA terminals, we initially hypothesized that SOM$^+$ interneurons may receive strong excitation from BLA. Surprisingly, however, only a fraction of SOM$^+$ interneurons receives monosynaptic excitation, and most fail to fire action potentials in response to light stimulation, arguing against a major role for SOM$^+$ interneurons in BLA-driven disynaptic inhibition. Although optical activation of ChR2-expressing BLA terminals may alter presynaptic release properties and short-term synaptic dynamics, particularly during repetitive stimulation, cells that exhibited light-evoked spiking had larger single-pulse oEPSCs than non-spiking cells, supporting an association between synaptic strength and postsynaptic recruitment. Given the heterogeneity of SOM$^+$ interneurons (Chamberland et al., 2024; Harris et al., 2018; Kinney et al., 2025; Losonczy et al., 2002; Yavorska and Wehr, 2016), whether SOM$^+$ interneurons targeted by BLA represent a specific subpopulation of SOM$^+$ interneurons remains an open question. Overall, our findings support a predominant role for PV$^+$ interneurons in feedforward inhibition driven by long-range glutamatergic inputs (Freund and Buzsaki, 1996; Li et al., 2023; Pelkey et al., 2017), whereas SOM$^+$ interneurons in CA1 and subiculum are more strongly associated with local feedback inhibition (Pouille and Scanziani, 2004).

BLA-CA3 versus BLA-CA1/subiculum pathways

Our previous work demonstrated that largely different populations of BLA neurons project to CA3 and CA1, suggesting that BLA input to these hippocampal subregions may represent partially segregated information channels rather than a uniform BLA signal distributed throughout the hippocampus (Li et al., 2025). Although we have not directly examined whether these two BLA populations are differentially activated during behavior, their anatomical segregation provides a potential mechanism by which BLA activity may differentially regulate hippocampal information processing through CA3 and CA1. In particular, the present findings suggest that the BLA→CA1/subiculum pathway can selectively activate specific populations of CA1/subiculum neurons, raising the possibility that BLA input may influence hippocampal processing at a later stage of the trisynaptic circuit.

The functional interaction between BLA→CA3 and BLA→CA1 pathways remains an important question to be studied in the future. Because these pathways arise largely from different BLA neuronal populations and target different hippocampal subregions, they could potentially provide complementary or coordinated regulation of hippocampal activity. At the same time, because distal CA3 and distal CA1–subiculum perform distinct computations and are interconnected within the hippocampal circuit, activation of these pathways could also

JNeurosci Accepted Manuscript

produce temporally distinct effects on hippocampal network activity. Our current experiments do not address this question, but rather that their anatomical segregation provides a substrate for pathway-specific modulation of hippocampal processing.

Reciprocal connections between BLA and ventral hippocampus

Taken together with previous studies (Felix-Ortiz et al., 2013; Felix-Ortiz and Tye, 2014; Hintiryan et al., 2021; Pi et al., 2020; Pikkarainen et al., 1999; Pitkanen et al., 2000; Yang and Wang, 2017), including our own (Li et al., 2025), our findings indicate that BLA–ventral hippocampal connectivity is highly complex at multiple levels. First, BLA does not indiscriminately target all pyramidal neurons in the ventral hippocampus. In both CA1 and CA3, BLA preferentially excites pyramidal neurons in distal segments (Li et al., 2025). These findings support the notion that ventral hippocampal CA1 and CA3 pyramidal neurons are functionally heterogeneous along the transverse axis (Sun et al., 2020a). Given that BLA plays a crucial role in emotion, anxiety, and social behaviors, it is reasonable to propose that the CA1 and CA3 subregions preferentially targeted by BLA (distal CA1 and distal CA3) may contribute disproportionately to these behaviors.

Second, BLA-mediated excitation of pyramidal neurons in vCA1–vSub is strongly regulated by feedforward inhibition, mediated primarily by PV^+ interneurons. This feedforward inhibitory pathway may therefore be an important component of functional interactions within amygdala–hippocampal circuits. Third, we found that pyramidal neurons receiving excitatory input from BLA also send reciprocal projections to BLA. Thus, the BLA–vCA1–vSub circuit may function as an extended recurrent network that enables bidirectional information exchange between interconnected limbic regions. Notably, in patients with temporal lobe epilepsy, the anterior hippocampus (equivalent to ventral hippocampus in rodents) and amygdala are frequently implicated in seizure generation (Aroniadou-Anderjaska et al., 2008; Babb et al., 1984; Bragdon et al., 1986; Ekstrand et al., 2011; Pitkanen et al., 1998). The recurrent excitatory connections in the BLA–vCA1–vSub circuit could potentially contribute to the susceptibility of this region to seizure generation. It should be noted that our retrograde tracing indicates that many pyramidal neurons in proximal vCA1 also project to BLA. However, proximal vCA1 neurons do not appear to receive direct BLA input. Finally, an important question for future studies is whether BLA neurons that project to the ventral hippocampus also receive direct excitatory input from the hippocampus. Such connectivity would provide an additional mechanism for reciprocal communication and potentially further strengthen the recurrent organization of this limbic circuit.

JNeurosci Accepted Manuscript

Author contributions

Conceptualization: M.L., Q.S; Data acquisition and data analysis: M.L., W.G., Y-Q. J., Q.S.; Figure preparation: M.L., W.G., Q.S.; Funding acquisition: Q.S.; Supervision: Q.S.; Writing: M.L., Q.S.

References

Alexander, G.M., Farris, S., Pirone, J.R., Zheng, C., Colgin, L.L., and Dudek, S.M. (2016). Social and novel contexts modify hippocampal CA2 representations of space. Nat Commun *7*, 10300.

AlSubaie, R., Wee, R.W., Ritoux, A., Mishchanchuk, K., Passlack, J., Regester, D., and MacAskill, A.F. (2021). Control of parallel hippocampal output pathways by amygdalar long-range inhibition. Elife *10*.

Amaral, D.G. (2003). The amygdala, social behavior, and danger detection. Ann N Y Acad Sci *1000*, 337-347.

Aroniadou-Anderjaska, V., Fritsch, B., Qashu, F., and Braga, M.F. (2008). Pathology and pathophysiology of the amygdala in epileptogenesis and epilepsy. Epilepsy Res *78*, 102-116.

Babb, T.L., Brown, W.J., Pretorius, J., Davenport, C., Lieb, J.P., and Crandall, P.H. (1984). Temporal lobe volumetric cell densities in temporal lobe epilepsy. Epilepsia *25*, 729-740.

Berretta, S., Munno, D.W., and Benes, F.M. (2001). Amygdalar activation alters the hippocampal GABA system: "partial" modelling for postmortem changes in schizophrenia. J Comp Neurol *431*, 129-138.

Bienkowski, M.S., Bowman, I., Song, M.Y., Gou, L., Ard, T., Cotter, K., Zhu, M., Benavidez, N.L., Yamashita, S., Abu-Jaber, J.*, et al.* (2018). Integration of gene expression and brain-wide connectivity reveals the multiscale organization of mouse hippocampal networks. Nat Neurosci *21*, 1628-1643.

Bragdon, A.C., Taylor, D.M., and Wilson, W.A. (1986). Potassium-induced epileptiform activity in area CA3 varies markedly along the septotemporal axis of the rat hippocampus. Brain Res *378*, 169-173.

Cembrowski, M.S., Bachman, J.L., Wang, L., Sugino, K., Shields, B.C., and Spruston, N. (2016). Spatial Gene-Expression Gradients Underlie Prominent Heterogeneity of CA1 Pyramidal Neurons. Neuron *89*, 351-368.

Cembrowski, M.S., and Spruston, N. (2019). Heterogeneity within classical cell types is the rule: lessons from hippocampal pyramidal neurons. Nat Rev Neurosci *20*, 193-204.

Chamberland, S., Grant, G., Machold, R., Nebet, E.R., Tian, G., Stich, J., Hanani, M., Kullander, K., and Tsien, R.W. (2024). Functional specialization of hippocampal somatostatin-expressing interneurons. Proc Natl Acad Sci U S A *121*, e2306382121.

JNeurosci Accepted Manuscript

578 Cope, E.C., Wang, S.H., Waters, R.C., Gore, I.R., Vasquez, B., Laham, B.J., and Gould, E.
579 (2023). Activation of the CA2-ventral CA1 pathway reverses social discrimination dysfunction in
580 Shank3B knockout mice. Nat Commun *14*, 1750.

581 Dudek, S.M., Alexander, G.M., and Farris, S. (2016). Rediscovering area CA2: unique
582 properties and functions. Nat Rev Neurosci *17*, 89-102.

583 Ekstrand, J.J., Pouliot, W., Scheerlinck, P., and Dudek, F.E. (2011). Lithium pilocarpine-induced
584 status epilepticus in postnatal day 20 rats results in greater neuronal injury in ventral versus
585 dorsal hippocampus. Neuroscience *192*, 699-707.

586 Fanselow, M.S., and Dong, H.W. (2010). Are the dorsal and ventral hippocampus functionally
587 distinct structures? Neuron *65*, 7-19.

588 Felix-Ortiz, A.C., Beyeler, A., Seo, C., Leppla, C.A., Wildes, C.P., and Tye, K.M. (2013). BLA to
589 vHPC inputs modulate anxiety-related behaviors. Neuron *79*, 658-664.

590 Felix-Ortiz, A.C., and Tye, K.M. (2014). Amygdala inputs to the ventral hippocampus
591 bidirectionally modulate social behavior. J Neurosci *34*, 586-595.

592 Freund, T.F., and Buzsaki, G. (1996). Interneurons of the hippocampus. Hippocampus *6*, 347-
593 470.

594 Gergues, M.M., Han, K.J., Choi, H.S., Brown, B., Clausing, K.J., Turner, V.S., Vainchtein, I.D.,
595 Molofsky, A.V., and Kheirbek, M.A. (2020). Circuit and molecular architecture of a ventral
596 hippocampal network. Nat Neurosci *23*, 1444-1452.

597 Guo, D., Wang, Z., Liu, F., Chen, W., Gao, X., Huang, S., Tabarak, S., Yao, Y., Zhang, S., Shi,
598 J.*, et al.* (2025). A ventral hippocampus-basolateral amygdala circuit regulates the
599 unconditioned stimulus retrieval-induced reconsolidation of remote fear memory. J Adv Res.

600 Harris, K.D., Hochgerner, H., Skene, N.G., Magno, L., Katona, L., Bengtsson Gonzales, C.,
601 Somogyi, P., Kessaris, N., Linnarsson, S., and Hjerling-Leffler, J. (2018). Classes and continua
602 of hippocampal CA1 inhibitory neurons revealed by single-cell transcriptomics. PLoS Biol *16*,
603 e2006387.

604 Hintiryan, H., Bowman, I., Johnson, D.L., Korobkova, L., Zhu, M., Khanjani, N., Gou, L., Gao, L.,
605 Yamashita, S., Bienkowski, M.S.*, et al.* (2021). Connectivity characterization of the mouse
606 basolateral amygdalar complex. Nat Commun *12*, 2859.

607 Hitti, F.L., and Siegelbaum, S.A. (2014). The hippocampal CA2 region is essential for social
608 memory. Nature *508*, 88-92.

609 Janak, P.H., and Tye, K.M. (2015). From circuits to behaviour in the amygdala. Nature *517*,
610 284-292.

611 Jiang, Y.Q., Lee, D.K., Guo, W., Li, M., and Sun, Q. (2024). Hypothalamic regulation of
612 hippocampal CA1 interneurons by the supramammillary nucleus. Cell Rep *43*, 114898.

JNeurosci Accepted Manuscript

Kim, W.B., and Cho, J.H. (2017). Synaptic Targeting of Double-Projecting Ventral CA1 Hippocampal Neurons to the Medial Prefrontal Cortex and Basal Amygdala. J Neurosci *37*, 4868-4882.

Kim, W.B., and Cho, J.H. (2020). Encoding of contextual fear memory in hippocampal-amygdala circuit. Nat Commun *11*, 1382.

Kinman, A.I., Kraus, L., and Cembrowski, M.S. (2026). The subiculum: cell-type-specific composition, computation, and function. Trends Neurosci *49*, 278-291.

Kinney, J.L., Robinson, H.L., Wang, H., Jiang, Y.Q., Zhou, M., Lee, D.K., Li, M., Oliva, A., and Sun, Q. (2025). Top-down regulation of subcortical regions by hippocampal long-range inhibition. Curr Biol *35*, 5853-5867 e5854.

Kjelstrup, K.G., Tuvnes, F.A., Steffenach, H.A., Murison, R., Moser, E.I., and Moser, M.B. (2002). Reduced fear expression after lesions of the ventral hippocampus. Proc Natl Acad Sci U S A *99*, 10825-10830.

Klausberger, T., and Somogyi, P. (2008). Neuronal diversity and temporal dynamics: the unity of hippocampal circuit operations. Science *321*, 53-57.

Li, M., Jiang, Y.Q., Lee, D.K., Wang, H., Lu, M.C., and Sun, Q. (2024). Dorsoventral Heterogeneity of Synaptic Connectivity in Hippocampal CA3 Pyramidal Neurons. J Neurosci *44*.

Li, M., Jiang, Y.Q., and Sun, Q. (2025). A circuit from the basolateral amygdala to hippocampal CA3 regulates social behavior. Curr Biol *35*, 4349-4364 e4345.

Li, M., Kinney, J.L., Jiang, Y.Q., Lee, D.K., Wu, Q., Lee, D., Xiong, W.C., and Sun, Q. (2023). Hypothalamic Supramammillary Nucleus Selectively Excites Hippocampal CA3 Interneurons to Suppress CA3 Pyramidal Neuron Activity. J Neurosci *43*, 4612-4624.

Losonczy, A., Zhang, L., Shigemoto, R., Somogyi, P., and Nusser, Z. (2002). Cell type dependence and variability in the short-term plasticity of EPSCs in identified mouse hippocampal interneurones. J Physiol *542*, 193-210.

Meira, T., Leroy, F., Buss, E.W., Oliva, A., Park, J., and Siegelbaum, S.A. (2018). A hippocampal circuit linking dorsal CA2 to ventral CA1 critical for social memory dynamics. Nat Commun *9*, 4163.

Moser, E., Moser, M.B., and Andersen, P. (1993). Spatial learning impairment parallels the magnitude of dorsal hippocampal lesions, but is hardly present following ventral lesions. J Neurosci *13*, 3916-3925.

Okuyama, T., Kitamura, T., Roy, D.S., Itohara, S., and Tonegawa, S. (2016). Ventral CA1 neurons store social memory. Science *353*, 1536-1541.

Oliva, A., Fernandez-Ruiz, A., Leroy, F., and Siegelbaum, S.A. (2020). Hippocampal CA2 sharp-wave ripples reactivate and promote social memory. Nature *587*, 264-269.

J Neurosci Accepted Manuscript

Pachicano, M., Mehta, S., Hurtado, A., Ard, T., Stanis, J., Breningstall, B., and Bienkowski, M.S. (2025). Laminar organization of pyramidal neuron cell types defines distinct CA1 hippocampal subregions. Nat Commun *16*, 10604.

Pelkey, K.A., Chittajallu, R., Craig, M.T., Tricoire, L., Wester, J.C., and McBain, C.J. (2017). Hippocampal GABAergic Inhibitory Interneurons. Physiol Rev *97*, 1619-1747.

Petreanu, L., Mao, T., Sternson, S.M., and Svoboda, K. (2009). The subcellular organization of neocortical excitatory connections. Nature *457*, 1142-1145.

Pi, G., Gao, D., Wu, D., Wang, Y., Lei, H., Zeng, W., Gao, Y., Yu, H., Xiong, R., Jiang, T., *et al.* (2020). Posterior basolateral amygdala to ventral hippocampal CA1 drives approach behaviour to exert an anxiolytic effect. Nat Commun *11*, 183.

Pikkarainen, M., Ronkko, S., Savander, V., Insausti, R., and Pitkanen, A. (1999). Projections from the lateral, basal, and accessory basal nuclei of the amygdala to the hippocampal formation in rat. J Comp Neurol *403*, 229-260.

Pitkanen, A., Pikkarainen, M., Nurminen, N., and Ylinen, A. (2000). Reciprocal connections between the amygdala and the hippocampal formation, perirhinal cortex, and postrhinal cortex in rat. A review. Ann N Y Acad Sci *911*, 369-391.

Pitkanen, A., Tuunanen, J., Kalviainen, R., Partanen, K., and Salmenpera, T. (1998). Amygdala damage in experimental and human temporal lobe epilepsy. Epilepsy Res *32*, 233-253.

Pouille, F., Marin-Burgin, A., Adesnik, H., Atallah, B.V., and Scanziani, M. (2009). Input normalization by global feedforward inhibition expands cortical dynamic range. Nat Neurosci *12*, 1577-1585.

Pouille, F., and Scanziani, M. (2001). Enforcement of temporal fidelity in pyramidal cells by somatic feed-forward inhibition. Science *293*, 1159-1163.

Pouille, F., and Scanziani, M. (2004). Routing of spike series by dynamic circuits in the hippocampus. Nature *429*, 717-723.

Sah, P., Faber, E.S., Lopez De Armentia, M., and Power, J. (2003). The amygdaloid complex: anatomy and physiology. Physiol Rev *83*, 803-834.

Strange, B.A., Witter, M.P., Lein, E.S., and Moser, E.I. (2014). Functional organization of the hippocampal longitudinal axis. Nat Rev Neurosci *15*, 655-669.

Sun, Q., Buss, E.W., Jiang, Y.Q., Santoro, B., Brann, D.H., Nicholson, D.A., and Siegelbaum, S.A. (2021). Frequency-dependent synaptic dynamics differentially tune CA1 and CA2 pyramidal neuron responses to cortical input. J Neurosci.

Sun, Q., Jiang, Y.Q., and Lu, M.C. (2020a). Topographic heterogeneity of intrinsic excitability in mouse hippocampal CA3 pyramidal neurons. J Neurophysiol *124*, 1270-1284.

Sun, Q., Sotayo, A., Cazzulino, A.S., Snyder, A.M., Denny, C.A., and Siegelbaum, S.A. (2017). Proximodistal Heterogeneity of Hippocampal CA3 Pyramidal Neuron Intrinsic Properties, Connectivity, and Reactivation during Memory Recall. Neuron *95*, 656-672 e653.

J Neurosci Accepted Manuscript

Sun, Y., Gooch, H., and Sah, P. (2020b). Fear conditioning and the basolateral amygdala. F1000Res *9*.

Watarai, A., Tao, K., Wang, M.Y., and Okuyama, T. (2021). Distinct functions of ventral CA1 and dorsal CA2 in social memory. Curr Opin Neurobiol *68*, 29-35.

Xiong, R., Li, B., Yu, H., Fan, T., Yu, H., Yang, Y., Wang, J.Z., Pi, G., and Yang, X. (2024). Urolithin A Inhibits Anterior Basolateral Amygdala to Ventral Hippocampal CA1 Circuit to Ameliorate Amyloid-beta-Impaired Social Ability. J Alzheimers Dis *99*, 1303-1316.

Xu, C., Krabbe, S., Grundemann, J., Botta, P., Fadok, J.P., Osakada, F., Saur, D., Grewe, B.F., Schnitzer, M.J., Callaway, E.M.*, et al.* (2016). Distinct Hippocampal Pathways Mediate Dissociable Roles of Context in Memory Retrieval. Cell *167*, 961-972 e916.

Yang, Y., and Wang, J.Z. (2017). From Structure to Behavior in Basolateral Amygdala-Hippocampus Circuits. Front Neural Circuits *11*, 86.

Yao, Z., van Velthoven, C.T.J., Nguyen, T.N., Goldy, J., Sedeno-Cortes, A.E., Baftizadeh, F., Bertagnolli, D., Casper, T., Chiang, M., Crichton, K.*, et al.* (2021). A taxonomy of transcriptomic cell types across the isocortex and hippocampal formation. Cell *184*, 3222-3241 e3226.

Yavorska, I., and Wehr, M. (2016). Somatostatin-Expressing Inhibitory Interneurons in Cortical Circuits. Front Neural Circuits *10*, 76.

Figure Legends

Figure 1. BLA projects to distal CA1 and subiculum in the ventral hippocampus.

(A) Experimental procedure and timeline. (B) Schematic illustrating the experimental procedure, in which the hippocampus was dissected and transverse sections were prepared along the dorsoventral axis. (C) Representative confocal images of transverse hippocampal sections spanning the dorsal-to-ventral axis. (D) Quantification of normalized fluorescence intensity of BLA fibers along the transverse axis from dorsal to ventral hippocampus. The horizontal dashed line indicates background noise, and the vertical dashed lines delineate hippocampal subregions (n = 4 mice). (E) Quantification of normalized fluorescence intensity of BLA fibers along the radial axis of vCA1a. The horizontal dashed line indicates background noise, and the vertical dashed lines delineate the different hippocampal layers (n = 4 mice). Shades show SEM.

Figure 2. CA1-projecting BLA neurons preferentially project to distal CA1 and subiculum in the ventral hippocampus.

Neurosci Accepted Manuscript

(A) Schematic indicating the site of AAVretro-Cre-mCherry injection in CA1 and Cre-dependent ChR2-eYFP injection in BLA. Bottom, experimental timeline. (B) Left: coronal section shows the expression of mCherry and ChR2-eYFP in BLA and hippocampus. Right: high-magnification confocal images of two co-labeled $mCherry^+/eYFP^+$ cells in BLA (arrows). (C) Schematic of experimental procedure showing that the hippocampus was dissected out and transverse sections were cut along the dorsoventral axis. (D) Confocal images of the transverse hippocampal sections spanning the dorsal-to-ventral axis. Expanded view of distal CA1 (CA1a) and subiculum (large orange box) in the ventral hippocampal section is shown in the far right. eYFP was pseudocolored black. (E) High-magnification confocal images of yellow squares from CA1 and subiculum shown in (D). (F) Quantification of normalized fluorescence intensity of BLA fibers along the transverse axis from dorsal to ventral hippocampus. Horizonal dashed line indicates the background noise. Vertical dashed lines delineate hippocampal subregions (n = 4 mice). (G) Quantification of normalized fluorescence intensity of BLA fibers along the longitudinal axis from dorsal to ventral (from 1 to 7) (n = 4 mice). (H) Quantification of normalized fluorescence intensity of BLA fibers from CA1a to CA1c in the hippocampus (n = 28 sections/4 mice). One-way ANOVA followed by Bonferroni's post hoc test. (I) Quantification of normalized fluorescence intensity of BLA fibers along the radial axis of vCA1a (n = 4 slices/4 mice). Horizonal dashed line indicates the background noise. Vertical dashed lines delineate different hippocampal layers. *$p < 0.05$; ***$p < 0.001$. Error bars and shades show SEM.

Figure 3. BLA input excites pyramidal neurons in distal vCA1 and vSub and largely avoids proximal vCA1 neurons.

(A) Experimental procedure and timeline. (B) Confocal images of biocytin-filled vCA1a and vSub neurons that underwent whole-cell recordings. Biocytin was pseudocolored black in left. (C) Sample voltage traces in response to indicated current injections in current-clamp from a vCA1a pyramidal neuron. (D) Group data of oEPSC amplitude recorded from vCA1-vSub neurons (n = 26 cells). Filled symbols indicate outliers. (E) Sample traces (left) and group data (right) of oEPSCs in voltage-clamp in the absence and presence of DNQX (20 μM) and DL-APV (50 μM) (n = 5 cells/4 mice, paired t test). (F) Sample traces (left) and group data (right) of oESPCs in voltage-clamp in baseline, after bath application of TTX (1 μM), and application of both TTX and 4-AP (100 μM) (n = 6 cells/4 mice, one-way ANOVA repeated measures). (G) Confocal images of biocytin-filled distal and proximal vCA1 neurons that underwent whole-cell recordings. Biocytin was pseudocolored black. (H-I) Sample traces (H) and group data (1) of oEPSCs recorded from CA1a and CA1c pyramidal neurons in voltage-clamp from the same slices (n = 5

JNeurosci Accepted Manuscript

pairs/4 mice, p = 0.024, paired t test). Blue bar indicates light pulse. *p < 0.05; **p < 0.01; ***p < 0.001. Error bars show SEM.

Figure 4. Stimulation of BLA terminals drives disynaptic inhibition in pyramidal neurons in vCA1-vSub.

(A) Sample traces of oEPSC (holding potential = -70 mV) and oIPSC (holding potential = 0 mV) in voltage clamp. (B) oIPSC amplitude plotted as function of oEPSC amplitude in individual cells (n = 7 cells/2 mice). The straight line indicates an I/E ratio of 1. (C) Expanded view of oEPSC and oIPSC traces denoted oEPSC and oIPSC onsets after light stimulation. Note the latency of oIPSC onset is greater than oEPSC. Blue bar indicates a 2-ms light pulse. (D) Group data of latency of oEPSC (n = 8 cells/2 mice) and oIPSC onsets (n = 8 cells/2 mice, unpaired t test). Blue bar indicates a 2-ms light pulse. (E-F) Sample oIPSC traces (E) and group data (F, n = 5 cells/2 mice, paired t test) in voltage clamp in the absence (black) and presence (red) of DNQX/APV. **p < 0.01. Error bars show SEM.

Figure 5. BLA excites interneurons in vCA1-vSub.

(A) Experimental procedure and timeline. (B) Sample confocal images of a hippocampal slice from a vGAT-td mouse that underwent whole cell recordings. Note four biocytin-filled cells (arrows) were co-labeled with tdTomato. Biocytin was pseudocolored black in left. (C) Volage traces from two interneurons in vCA1-vSub in response to indicated current injections in current clamp. (D) Sample light-evoked EPSCs. Blue bars indicate light pulses. Black and grey traces represent mean and individual traces, respectively. Note small jigger of oEPSC onsets in response to light pulses in putative monosynaptic connections (top) and longer and variable oEPSC onsets in putative polysynaptic connections (bottom). (E) Group data of latency of oEPSC onsets (short latency: n = 21 cells/6 mice; long latency: n = 11 cells/6 mice; unpaired t test). The blue bar indicates a 2-ms light pulse. (F) Group data of jitter of oEPSC onsets (short latency: n = 11 cells/5 mice; long latency: n = 5 cells/3 mice; unpaired t test). (G-H) Sample voltage traces (G) and group data of spike probability (H, n = 25 cells/7 mice) of suprathreshold APs evoked by a train of 20 Hz light stimulation in current clamp. ***p < 0.001. Error bars show SEM.

Figure 6. BLA strongly excites PV^+ interneurons in vCA1–vSub.

(A) Top, schematic showing the genetic approach to label PV^+ cells with tdTomato. Bottom, experimental procedure and timeline. (B) Sample confocal images of a hippocampal slice from a

JNeurosci Accepted Manuscript

PV-td mouse that underwent whole cell recordings. Note three biocytin-filled cells. Biocytin was pseudocolored black in left. (C) Sample voltage traces from a PV^+ cell in response to indicated current injections in current clamp. Note fast spiking in response to positive current injections. (D-E) Sample traces (D) and group data (E) of oESPCs in voltage-clamp in baseline, after bath application of TTX (1 μM), and application of both TTX and 4-AP (100 μM) (n = 4 cells/2 mice). (F) Group data of probability of putative monosynaptic connections between BLA and PV^+ cells and between BLA and vCA1–vSub interneurons. Numbers of cells are shown above the bars. (G) Group data of oEPSC amplitude in PV^+ cells (n = 14 cells/4 mice) and CA1 interneurons (n = 21 cells/7 mice). Filled symbols indicate outliers. Mann-Whitney U test. (H) Group data of the percentage of PV^+ cells and CA1 interneurons that fire APs in response to single light pulses. Numbers of cells are shown above the bars. (I-J) Sample voltage traces (I) and group data of spike probability (J) of suprathreshold APs evoked by a train of 20 Hz light stimulation in current clamp (PV^+: n = 10 cells/4 mice, interneurons: n = 11 cells/7 mice, only responsive cells included). Two-way ANOVA repeated measures. ***$p < 0.001$. Error bars show SEM.

Figure 7. BLA weakly excites a small subset of SOM^+ interneurons in vCA1–vSub.

(A) Top, schematic showing the genetic approach to label SOM^+ cells with tdTomato. Bottom, experimental procedure and timeline. (B) Sample confocal images of a hippocampal slice from a SOM-td mouse that underwent whole cell recordings. Note three biocytin-filled cells in SO. Biocytin was pseudocolored black in left. (C) Sample volage traces from two SOM^+ cells in response to indicated current injections in current clamp. Left shows a regular-spiking cell and right shows a cluster-firing cell. (D) Sample current traces from a nonresponsive cell (top) and a responsive cell (bottom) in voltage clamp. (E) Sample voltage traces from a nonresponsive cell (top) and a responsive cell (bottom) in current clamp. (F-H) Summary data of probability of putative monosynaptic connections (F), oEPSC amplitude (G), and percentage of cells showing light-evoked spikes (H) from PV^+ cells (n = 4 mice), SOM^+ cells (n = 2 mice), and vCA1–vSub interneurons (n = 7 mice). Numbers of cells are shown above the bars. Filled symbols indicate outliers. Kruskal-Wallis test in (G), Chi-square test, Fisher's exact test and post-hoc pairwise comparisons in (H). *$p < 0.05$, ***$p < 0.001$.

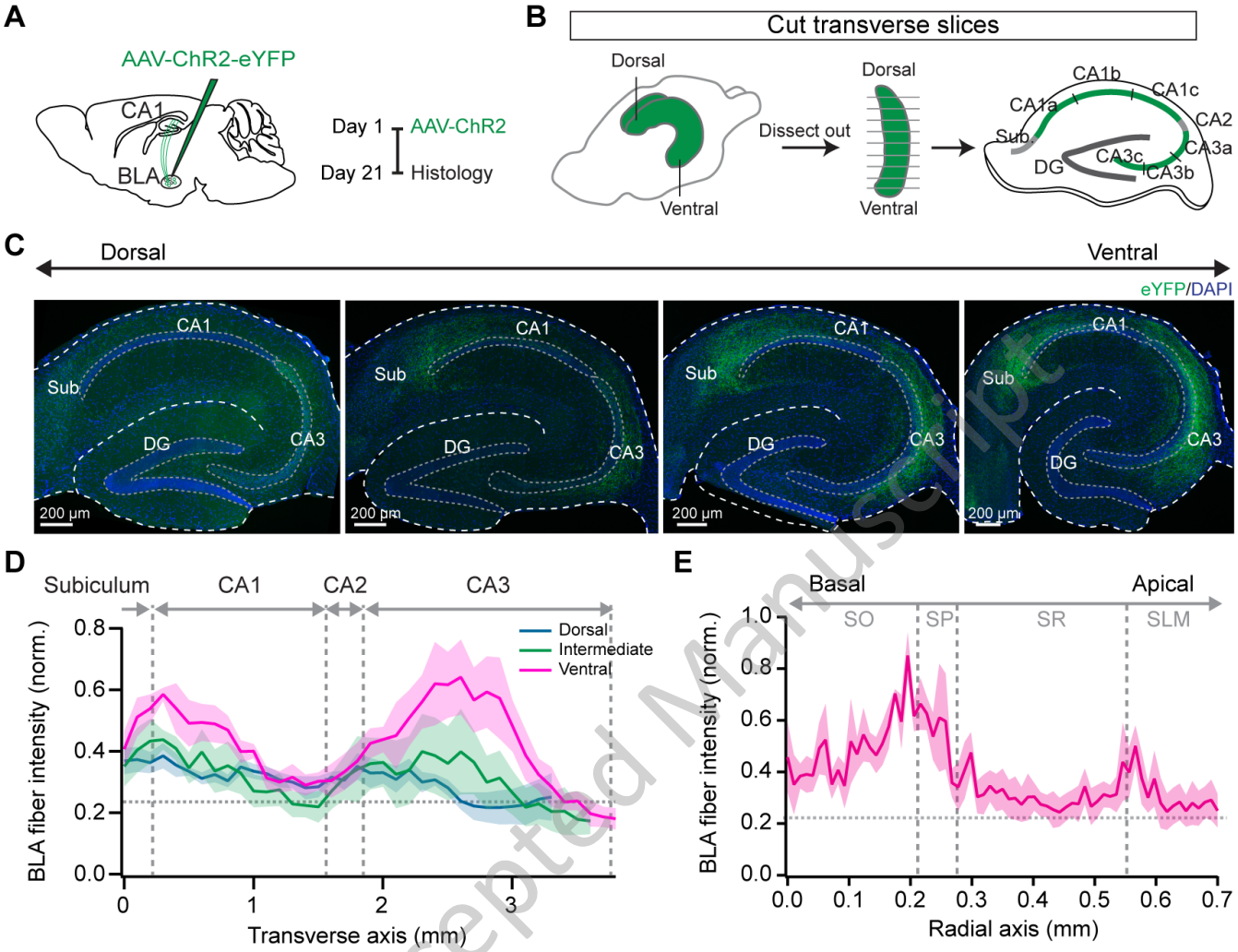
Figure 8. Pyramidal neurons in vCA1-vSub both receive excitation from and project to BLA.

(A) Schematic of two possible models of reciprocal connections between vCA1-vSub and BLA. Left shows that the same neurons in vCA1-vSub both receive excitation from and project to

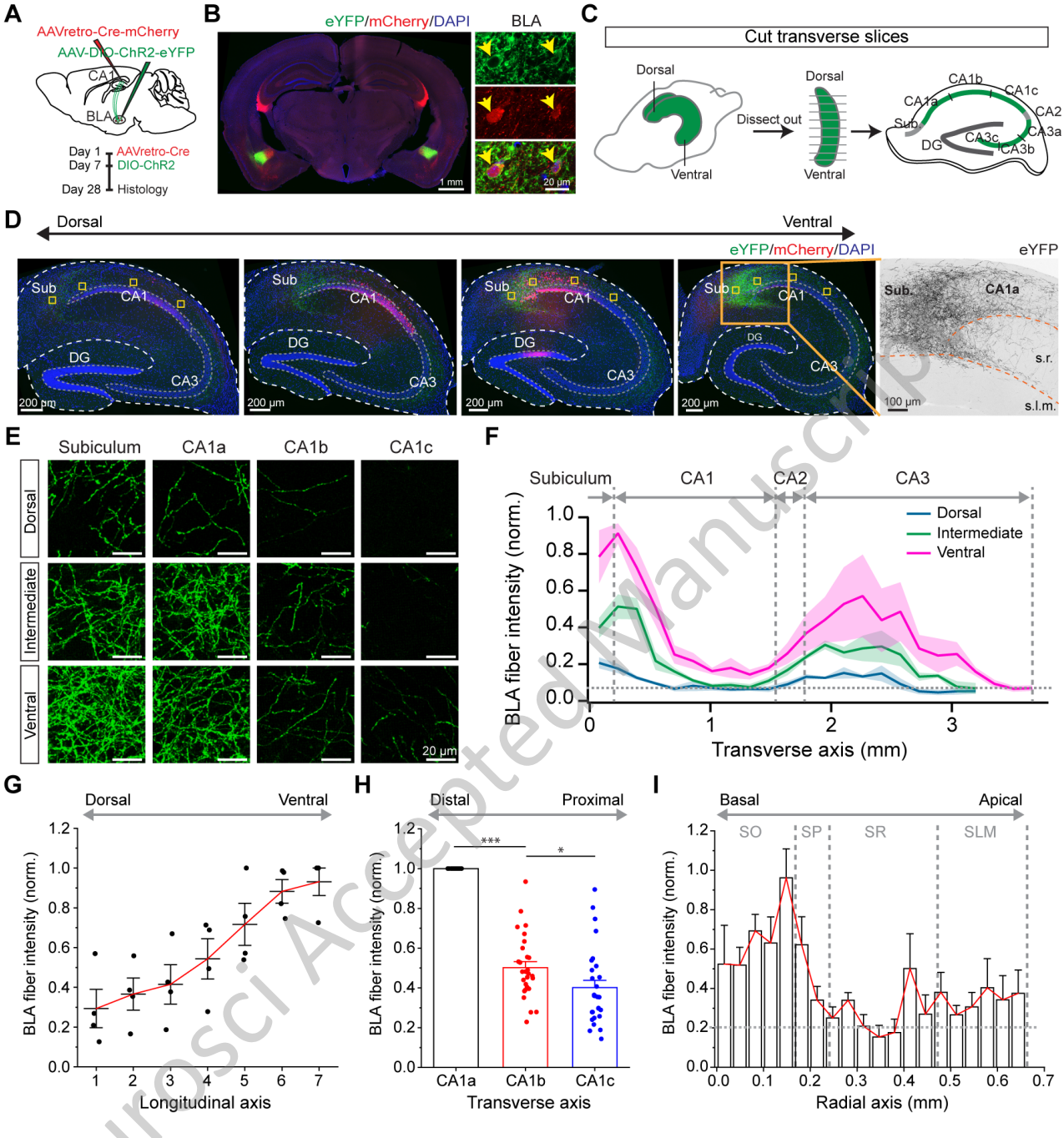
Neurosci Accepted Manuscript

BLA. Right shows that neurons in vCA1-vSub projecting to BLA differ from those that receive BLA input. (B) Experimental procedure and timeline. (C) Confocal images show the injection site of mixed AAVretro-H2B-mCherry and AAV-ChR2-eYFP in the coronal section (left) and expanded view in BLA (right). (D) Confocal images of coronal section at Bregma -3.1 mm. Expanded views of blue box are shown in the right. Note numerous $mCherry^+$ cells but few $ChR2\text{-}EYFP^+$ fibers. (E) Confocal images of coronal section at Bregma -3.5 mm. Expanded views of orange box are shown in the right. Note the overlap of $mCherry^+$ cells and $ChR2\text{-}EYFP^+$ fibers. (F) A confocal image of a transverse slice from the ventral hippocampus. (G) Sample confocal images of a biocytin-filled vSub pyramidal neuron that underwent whole-cell recording. The cell is positive for mCherry. (H) Membrane voltage in responses to indicated somatic current injections from a regular-spiking (left) and burst firing neurons (right) in current clamp. Inset shows the expanded view of a burst from the dashed gray box. (I-J) Sample voltage clamp recording trace (I) and summary data of oEPSCs (J, n = 10 cells/2 mice).

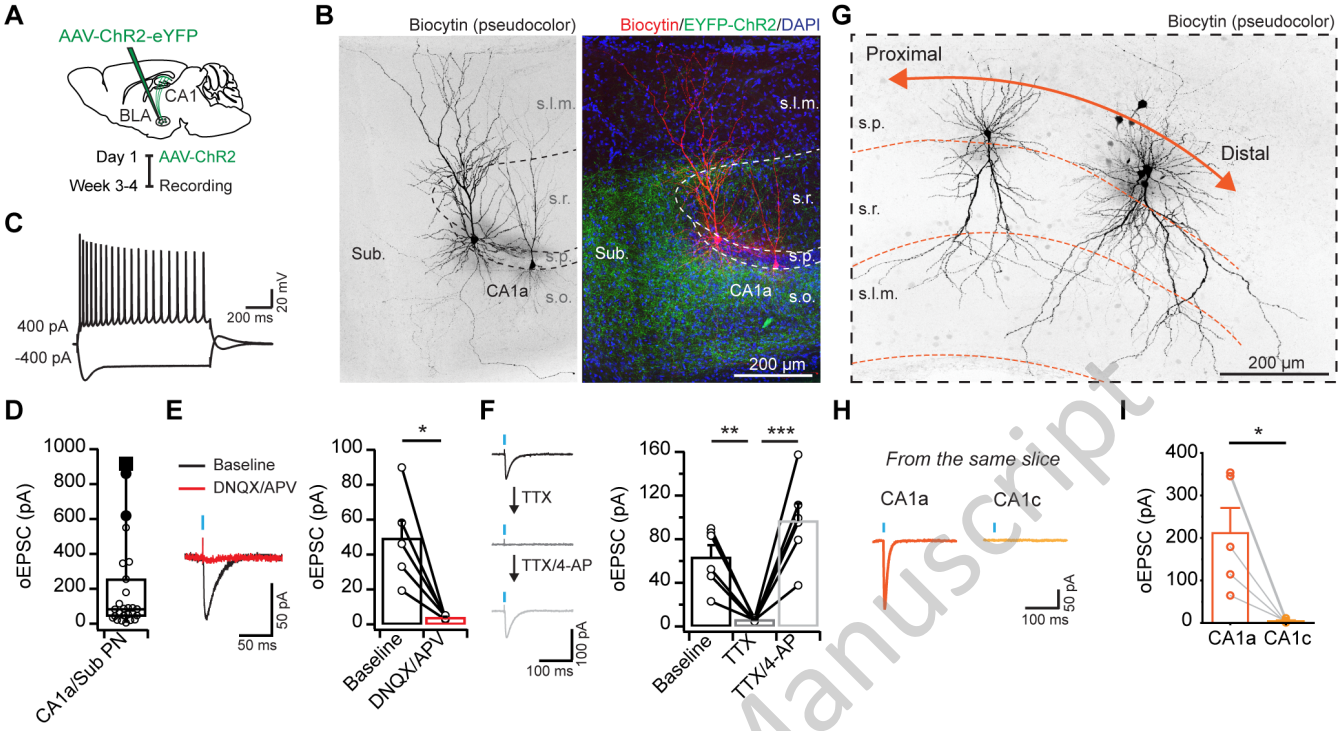
JNeurosci Accepted Manuscript



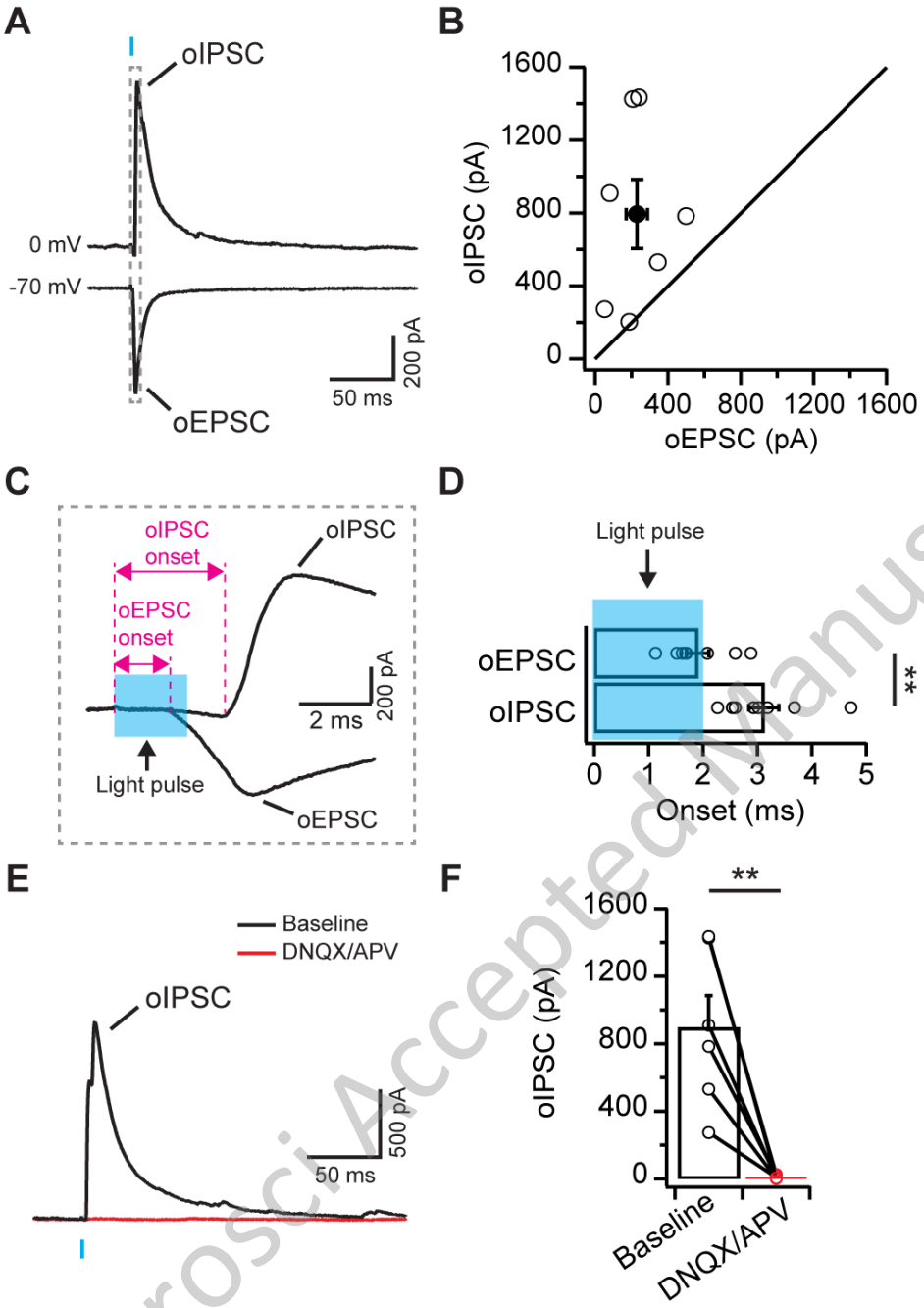
JNeurosci Accepted Manuscript



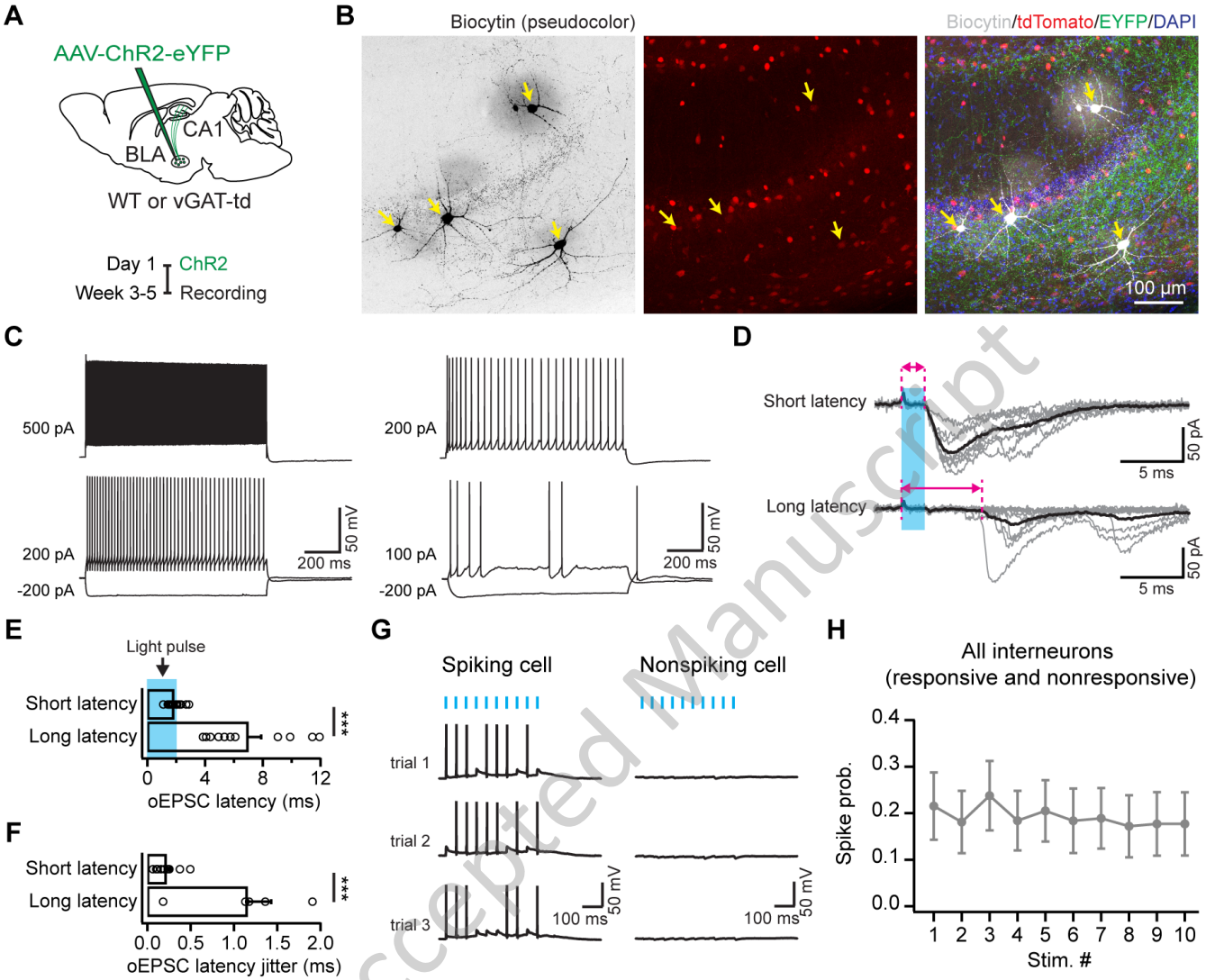
JNeurosci Accepted Manuscript



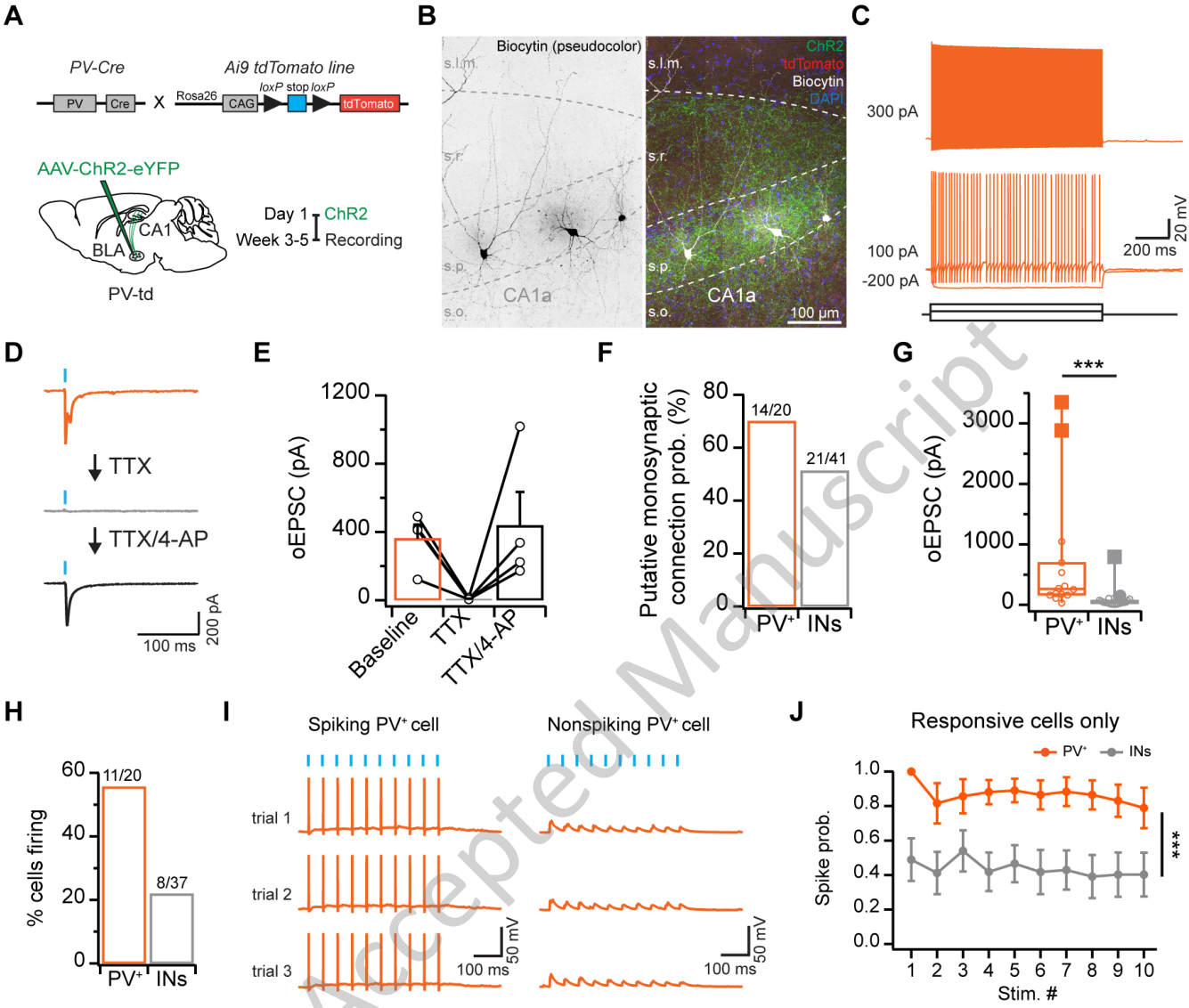
JNeurosci Accepted Manuscript



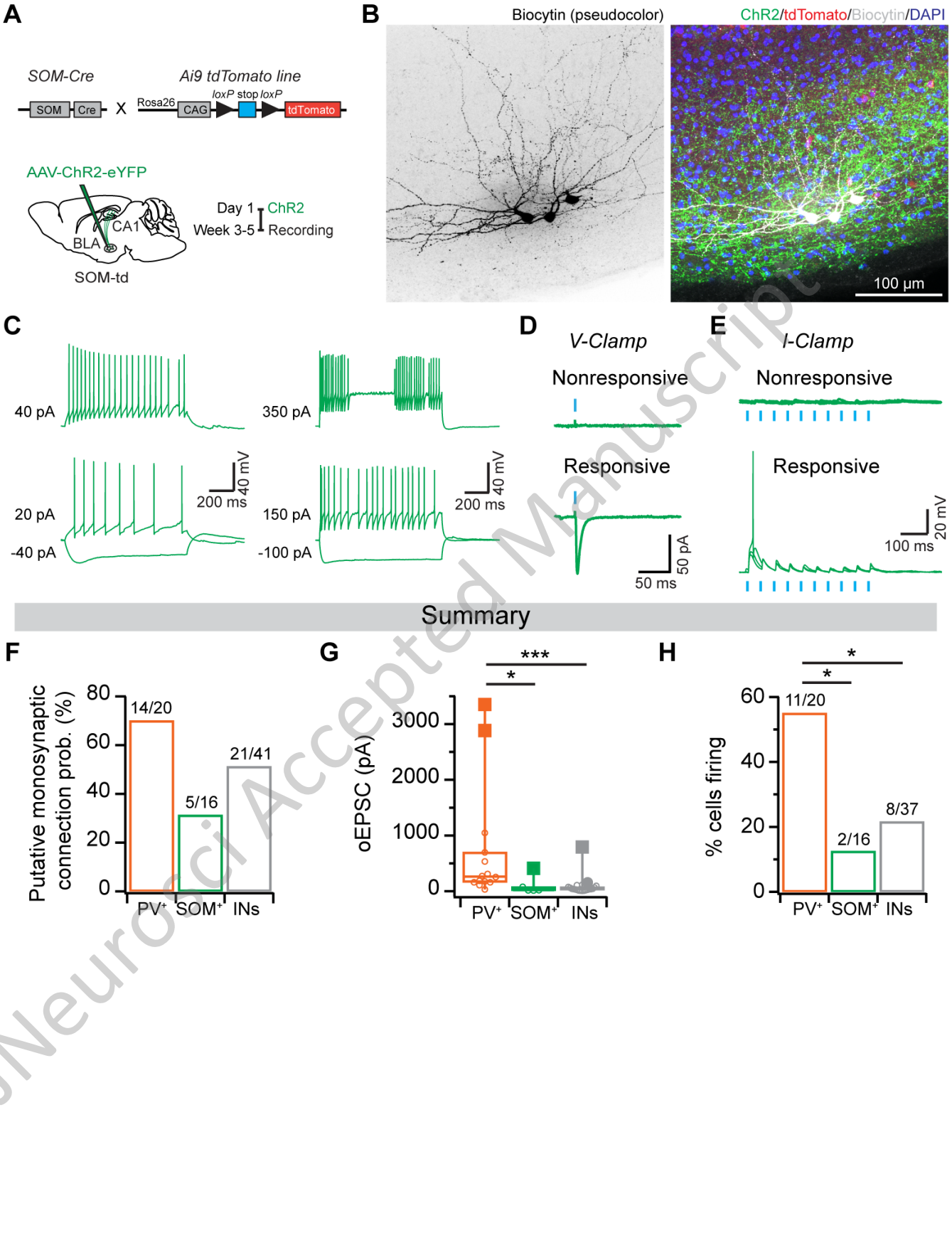
JNeurosci Accepted Manuscript



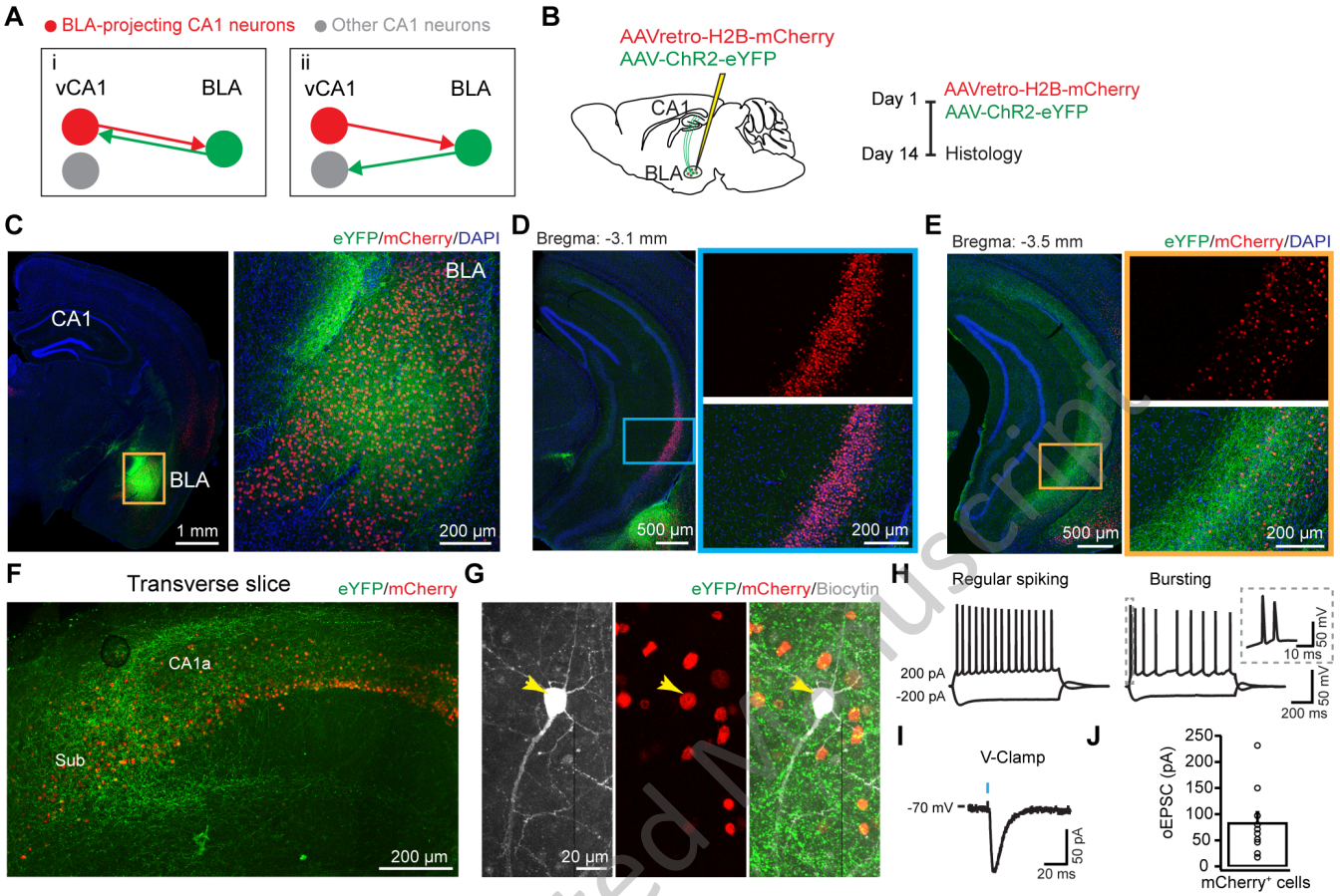
JNeurosci Accepted Manuscript



JNeurosci Accepted Manuscript



JNeurosci Accepted Manuscript



JNeurosci Accepted Manuscript